ACS OMEGA

Open Access

http://pubs.acs.org/journal/acsodf

Article

Mapping the Binding Hotspots and Transient Binding Pockets on V-Domain Immunoglobulin Suppressor of T Cell Activation Protein Surface

Bingjie Li, Lixiu Xu, Chu Chen, and Jiqing Ye*

Cite This: *ACS Omega* 2024, 9, 48657−48669

Read Online

ACCESS | Metrics & More | Article Recommendations | Supporting Information

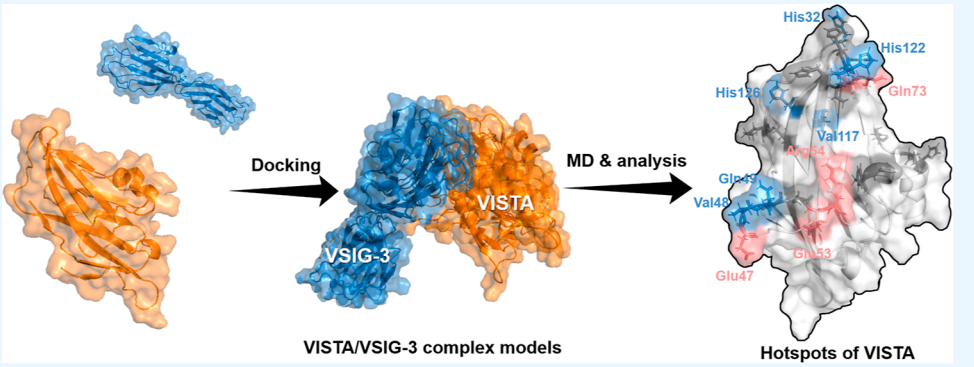

ABSTRACT: V-domain immunoglobulin suppressor of T cell activation (VISTA), an inhibitory immune checkpoint present on both immune and tumor cells, has emerged as a highly promising target for cancer therapy due to its potential to overcome resistance encountered with existing immune checkpoint treatments. VSIG-3 is determined as an inhibitory ligand for VISTA, leading to the suppression of T cell proliferation. However, hotspots between VISTA/VSIG-3 protein−protein interaction remain ambiguous, mainly attributed to the lack of the structure of the VISTA/VSIG-3 complex. Therefore, in this study, in order to determine the energetic contributions of the interfacial residues on VISTA, we first constructed VISTA/VSIG-3 complex models by the protein docking method, followed by molecular dynamics simulations, binding free-energy decomposition, and alanine scanning. Results suggested that the putative hotspots in VISTA comprise residues His32, Tyr37, Thr35, Glu47, Val48, Gln49, Glu53, Arg54, Gln73, His122, and His126. Moreover, the distribution of the hotspots was clustered into two regions (hot regions I and II), and by using the TRAPP tool, transient subpockets within the hot regions were identified. Furthermore, conformational states of the binding pockets exhibiting druggability scores higher than those observed in the crystal structure were found. Overall, we hope that the findings outlined in this study can be used to facilitate the development of inhibitors targeting the VISTA/VSIG-3 immune checkpoint pathway in the future.

1. INTRODUCTION

Cancer immunotherapy has made significant progress since the introduction of the concepts of immunological surveillance and cancer immunoediting.[1] Unlike conventional treatments, the fundamental principle of immunotherapy is that it stimulates the patient's own immune system to combat cancer rather than directly eliminates tumor cells via anticancer drugs or physical interventions.[2] During the immune response against tumor cells, T cells can recognize specific antigens presented by antigen-presenting cells (APCs) and acquire effector functions to eliminate the tumor cells.[3]

Immune checkpoints are crucial for regulating immunological response, maintaining systemic immune homeostasis by restricting T cell activation, as well as avoiding immune system damage to peripheral organs.[4] After the initial discovery of immune checkpoints, including CTLA-4 and PD-1/PD-L1, several other Ig superfamily T cell inhibitory ligands/receptors, such as LAG3, TIM3, VISTA, etc., have been identified as significant regulators of antitumor immunity.[5] FDA-approved monoclonal antibodies (mAbs) targeting CTLA-4 or PD-1/PD-L1, including Nivolumab, Pembrolizumab, Atezolizumab, and Ipilimumab, have demonstrated the clinical success of immune checkpoint inhibitors.[6] Despite their clinical success, monoclonal antibodies (mAbs) have limitations such as poor permeability, limited oral bioavailability, high cost, insufficient

Received: August 22, 2024
Revised: November 2, 2024
Accepted: November 18, 2024
Published: November 23, 2024

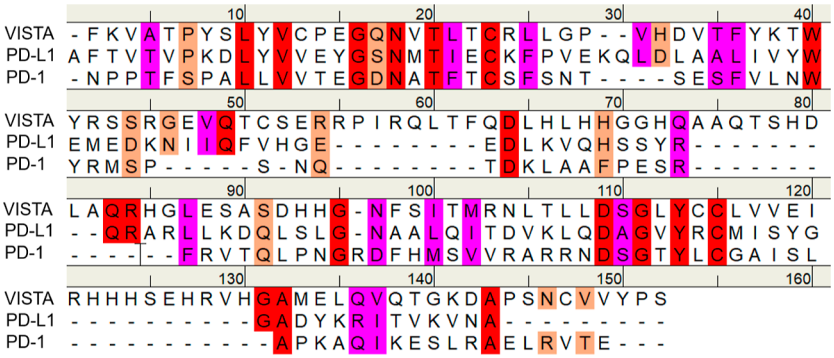

Figure 1. Sequence alignment of IgV domains of B7 family member VISTA (PDB: 6OIL) with CD28/B7 family members PD-1/PD-L1, respectively (PDB: 4ZQK). Identical, strong, and weak similarity residues are highlighted red, magenta, and orange, respectively.

half-life, and immune-related adverse events, with overall response rates in solid tumor patients typically below 30%.[7] Therefore, current immunotherapy targets are insufficient to meet clinical needs, and it is necessary to identify novel therapeutic targets to boost antitumor immunity.

V-domain Ig suppressor of T cell activation (VISTA) protein, a member of the B7 superfamily, is an inhibitory immune checkpoint highly expressed on mature CD11b high myeloid-derived antigen-presenting cells (APCs) and to a lesser extent on $CD4^+$, $CD8^+$, and regulatory T cells and also found on tumor-infiltrating lymphocytes.[8] VISTA has been considered as one of the most appealing targets for cancer therapy for overcoming resistance to current immune checkpoint therapies.[9] Several proteins have been reported to be VISTA binding partners. Among these, VSIG-3 and PSGL-1 are two confirmed binding partners with immunosuppressive roles, while VSIG-8 and Gal-9 are considered less established binding partners.[10] VSIG-3 acts as an inhibitory ligand for VISTA, leading to the suppression of T cell proliferation, cytokine, and chemokine production upon engagement with activated T cells.[11] The coinhibitory effects of VSIG-3 on activated T cells, coupled with its significantly heightened expression in colorectal cancers, hepatocellular carcinomas, and intestinal-type gastric cancers, indicate that targeting the VSIG-3/VISTA pathway could serve as a novel strategy for cancer immunotherapy.[12]

The human VISTA protein consists of 279 amino acids, including a 162-amino-acid extracellular domain, 21-amino-acid transmembrane domain, and a 96-amino-acid cytoplasmic domain.[13] Protein sequence analysis reveals that VISTA shares a conserved immunoglobulin variable (IgV)-like fold with other B7 family members.[13] Among these, PD-L1 is the closest B7 family homologue to VISTA, sharing 22% sequence identity.[14] Moreover, VISTA also shares homology with the T cell coinhibitory receptor PD-1, which belongs to the CD28 superfamily[15] (Figure 1). The human VISTA (hVISTA) extracellular domain crystal structure was reported by Cochran et al. in 2019.[16] However, there is no crystal structure of the VISTA/VSIG-3 complex published yet. In order to identify the epitopes for VSIG-3 on VISTA, mutagenesis studies were performed. In the work by Cochran et al., three residues from the CC′ loop (Arg54, Phe62, and Gln63) are confirmed as key residues interacted with VSIG-3 by the mutant study.[16] However, the mutagenesis yielded some contradictory results in different studies. For example, in the latest work by Cochran et al., mutation of Phe62 into Ala increased the binding of VSIG-3 to VISTA.[17] Moreover, they recognized that residues 36−39 from the C-strand are heavily involved in the interaction with VSIG-3, but not all of the determined residues (e.g., Phe36, Lys38, etc.) are surface-exposed to allow for binding.[17] Therefore, more studies should be performed to further elucidate the architecture of the hotspots in the VISTA/VSIG-3 interfaces.

As an attractive substitute for in vitro assays, molecular dynamics (MD) simulations, incorporating physical principles and computational methodologies like free-energy simulation, alanine scanning, offer essential dynamic and thermodynamic insights crucial for understanding biomolecular complexes.[18] For example, computational methods have been successfully applied to the PD1/PD-L1 system, providing a wealth of profound insights into understanding the interaction between PD1 and PD-L1, such as the hotspot determination, conformational changes of loop regions, structural properties of interfaces, and so forth.[19]

In this work, we focused on the characterization of VISTA hotspots that are crucial for the interaction with VSIG-3. Due to the absence of a VISTA/VSIG-3 complex crystal structure, protein−protein docking was employed to generate multiple complex models as initial points for MD simulations. Subsequently, calculations and analyses of the binding free energy of the interfacial residues were conducted. Moreover, the energetic contribution of individual residues was assessed using per-residue energy decomposition and alanine scanning. The distribution of energetic contributions from residues across the VISTA interface was then clustered to display the hot regions. Furthermore, the dynamics of the hot regions were examined using TRAPP ("Transient Pockets in Proteins"), revealing "transient" subpockets in these regions.[20,21] Finally, conformational states of the hot regions with druggability scores higher than those of the crystal structure were identified, potentially offering guidance for the structure-based design of novel small-molecule binders.

2. MATERIALS AND METHODS

2.1. Structure Preparation. Coordinates of the VISTA crystal structure (PDB ID: 6OIL) were retrieved from the Protein Data Bank (https://www.rcsb.org/structure). The three-dimensional structure of VSIG-3 (Uniport ID: Q5DX21) was downloaded from AlphaFold (https://alphafold.ebi.ac.uk/entry/Q5DX21), and the protein domain (residues 23−233) was retained in the structure, and the rest of the atoms were deleted. Both structures were preprocessed by the protein preparation tool implemented in Discovery Studio 2017 (DS2017). Water and heteroatoms were removed,

https://doi.org/10.1021/acsomega.4c07757
ACS Omega 2024, 9, 48657−48669

hydrogens were added, side chains were refined, and missing loops were predicted with Looper under the CHARMm force field, and the residues were protonated at pH 7.4.

2.2. VISTA/VSIG-3 Complex Modeling. VISTA/VSIG-3 complex was constructed using the ZDOCK module implemented in DS2017. The three-dimensional modeled structure of VSIG-3 IgV domain was docked to the crystal structure of the VISTA IgV domain. The angular step size was set to 6 to obtain finer conformational sampling and more accurate predictions. Filtering of the docked poses was done by selecting residues Arg54, Phe62, Gln63, and Ile119 from VISTA presented in the receptor binding sites. Top 2000 poses ranked by the ZRank score were retained and clustered, with both the root-mean-square deviation (RMSD) cutoff and interface cutoff set to 10 Å. Subsequently, unreasonable poses were deleted manually, resulting in 439 poses. The selected structures were refined using the RDOCK tool in DS2017. All the refined models were aligned to the structure of PD-1/PD-L1 (PDB: 4ZQK) based on main-chain atoms and secondary structures using Align and Superimpose Proteins tool in DS2017. RMSDs between the PD-1/PD-L1 experimental complex and the constructed models were calculated. The distribution of all models was graphed based on RMSDs plotted versus ZRank scores. Three models, including model_3 with the lowest ZRank score, model_243 with the lowest RMSD value, and model_82 with a balanced ZRank score and RMSD value, were selected for further analysis.

2.3. Residue Interaction Network (RIN) Diagram. Numerous research endeavors have employed RINs as a valuable tool for comprehensively delineating and examining diverse classes of intra- or intermolecular interactions, thereby facilitating the acquisition of meaningful insights into intricate biological phenomena. Therefore, in this study, the protein−protein RINs were derived via the utilization of the RING web server (https://ring.biocomputingup.it/submit).[22] The three retained VISTA/VSIG-3 models were fed into the server at strict distance thresholds for various interactions, such as hydrogen bonding, ionic interaction, π-cation, and so forth. The residues and the interactions between residues represented as nodes and edges, respectively, were generated from the server. The interfacial RINs were extracted, visualized, and reconstructed in Cytoscape 3.9.1.

2.4. MD Simulations. To study the molecular interactions of VISTA with VSIG-3, the three VISTA/VSIG-3 models together with the apo form structure of VISTA ($VISTA_{apo}$) were subjected to MD simulations with the GROMACS-2020.3 package under the OPLS-AA/L force field. The topology parameters and coordinates of proteins were created by GROMACS-2020.3 program. The systems were contained in a cubic box of simple point charge water molecules and maintained a solute−box distance of 1.0 nm. The solvated systems were neutralized by adding counterions including sodium (Na^+) and chloride (Cl^-) ions. The steepest descent minimization algorithm with a tolerance value of 1000 kJ/mol/nm was used to minimize the systems. After convergence, the systems were subjected to *NVT* and *NPT* ensemble MD simulations for 1000 ps, successively. A modified Berendsen thermostat and a Parrinello−Rahman barostat were applied to keep the temperature and pressure constant at 300 K and 1 bar, respectively. The particle mesh Ewald method was used to calculate the long-range electrostatic interactions. Finally, unrestrained 800 ns production simulations were carried out under constant pressure and temperature conditions. Following the completion of the simulation, RMSD and root-mean-square fluctuation (RMSF) were computed by utilizing the tools provided by the GROMACS package.

2.5. Binding Free-Energy Calculations. Dynamic profiles of VISTA/VSIG-3 models were taken to calculate the binding free energy. The molecular mechanics (MM) Poisson−Boltzmann surface area (MM-PBSA) approach of the gmx_MMPBSA package[23] was used for calculation. Amberff14SB force field with other default parameters were applied for all calculations. Five hundred snapshots extracted every 0.8 ns from the last 400−800 ns equilibration region of the trajectory were used for the calculation of average binding free energy. The following equations were used to calculate the binding free energy (ΔG_{bind})

$$\Delta G_{bind} = \Delta G_{complex} - (\Delta G_{receptor} + \Delta G_{ligand})$$

$$\Delta G_{bind} = \Delta E_{MM} + \Delta E_{PB} + \Delta E_{SASA} - T\Delta S$$

$$\Delta E_{MM} = \Delta E_{bonded} + \Delta E_{nonbonded}$$

$$=(\Delta E_{bond} + \Delta E_{angle} + \Delta E_{dihedral}) + (\Delta E_{ele} + \Delta E_{vdw})$$

In the aforementioned equations, the vacuum potential energy (ΔE_{MM}), calculated based on the MM force field, represents the changes in molecular mechanical energy in the gas phase, comprising ΔE_{bonded} (internal energy) and $\Delta E_{nonbonded}$ (contributions from van der Waals and electrostatic forces). ΔE_{PB} is the polar solvation contribution calculated by solving the Poisson−Boltzmann (PB) equation, while the nonpolar component is usually assumed to be proportional to the molecule's total solvent accessible surface area. $-T\Delta S$ denotes the conformational entropy after ligand binding, which is usually calculated by normal-mode analysis (NMODE). In this study, entropy component was estimated for 100 snapshots taken from the last 400 ns trajectories by using the NMODE method. Generally, the calculation of entropy typically is time-consuming. Therefore, when calculating the binding free energy, entropy is usually not considered, and the binding free energy (ΔG_{bind}) without considering entropy is denoted by enthalpy (ΔH or $\Delta G_{bind}^{substoal}$).

2.6. Energy Decomposition and Computational Alanine Scanning. The PB model was utilized to compute the binding free-energy contributions of each amino acid at the interface between the PPIs. This calculation was performed on the same 500 snapshots extracted from the trajectory previously employed for the binding free-energy calculation, providing a comprehensive understanding of the interactions between VISTA and VSIG-3. To validate the hotspots in the VISTA interface identified by the free-energy decomposition method, a computational alanine scanning approach was conducted, selectively mutating key residues to alanine based on a cutoff of −1.00 kcal/mol in energy contribution to the binding energy, excluding alanine and proline residues. The mutated residues were those that played a crucial role in the interaction and were involved in the PPI. Subsequently, the binding free energy was recalculated at both the residue level and the overall structural level, assuming that local changes would not significantly impact the overall conformation of the complexes. Finally, the changes in the binding free energies of the mutant and wild-type systems, $\Delta\Delta G_{bind}$, were calculated through the following formula: $\Delta\Delta G_{bind} = \Delta G_{bind}^{mut} - \Delta G_{bind}^{wild}$. The positive values of $\Delta\Delta G_{bind}$ denote the favorable or important contribution of the residue in the complex

https://doi.org/10.1021/acsomega.4c07757
ACS Omega 2024, 9, 48657−48669

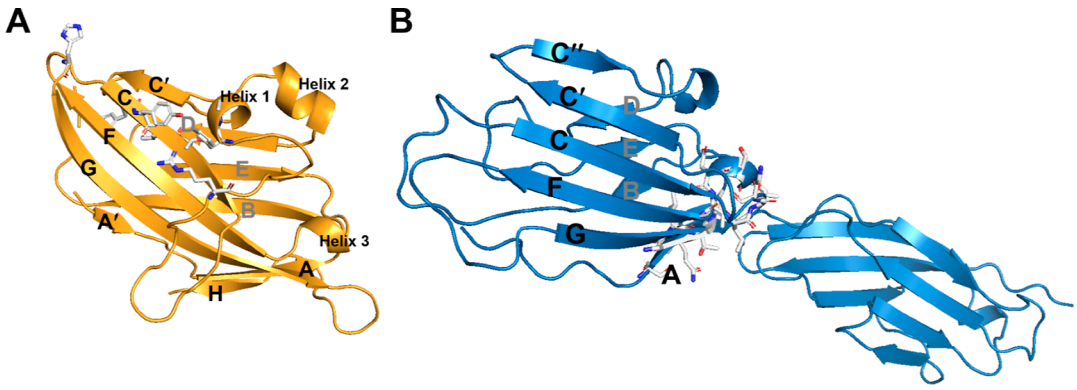

Figure 2. Proposed interfaces of VISTA/VSIG-3. (A) Cartoon structure of VISTA is colored bright orange, with the proposed interface composed of G-, F-, C′-, and C-strands. (B) VSIG-3 is colored sky blue, with the proposed interface composed of C-, C′-, C″-, F-, and G-strands. Residues affecting the VISTA/VSIG-3 interaction, as identified by mutagenesis studies, are shown in stick.

association, whereas negative values indicate unfavorable or trivial contributions.

2.7. Analysis of Transient Binding Pockets in Hot Regions Using TRAPP. Transient binding pockets within the hot regions of VISTA were assessed utilizing the TRAPP (*Transient Pockets in Proteins*) web server (https://trapp.h-its.org/trapp), a tool designed for the analysis of variations of binding pockets along the protein trajectory.

Snapshots were extracted at 2 ns intervals from the MD trajectory of the apo VISTA protein (PDB: 6OIL), resulting in a total of 400 snapshots for the TRAPP analysis. Structures were aligned and superimposed onto the reference structure (the experimentally determined structure of VISTA) using the backbone atoms. Within hot region I, the binding site was centered at coordinates 26.270, 26.342, and 37.478 (x, y, z), encompassing a radius of 12 Å from the central point. In hot region II, the binding site was defined with central coordinates of 25.886, 46.858, and 45.000 (x, y, z) and a radius of 9 Å. TRAPP provides "conserved" and "transient" pocket regions. The conserved pocket regions were defined as those observed in the reference structure and in at least 80% occurrence. "Transient" pocket regions are defined as pockets that appear/disappear relative to the reference structure. In our analyses, we identified "transient" subpocket regions that appear or disappear in at least 50% of snapshots. Finally, druggability score values of binding pockets detected in the "reference structure" and snapshots extracted from the trajectory were calculated using logistic regression (LR) and convolutional neural network (CNN) models, respectively.

3. RESULTS

3.1. Proposed VISTA/VSIG-3 Interfaces. The canonical fold of the B7 family comprises two distinct domains: an IgV domain with nine beta strands and an immunoglobulin constant (IgC) domain with seven beta strands.[24] Typically, the IgC domain is proximal to the membrane, while the IgV domain is distal and interacts directly with its cognate receptor. In 2019, Cochran et al. reported the crystal structure of the $hVISTA_{apo}$ IgV domain for the first time, and it was observed to have 10 beta strands and three alpha helices arranged in a canonical beta-sandwich formation[16] (Figure 2). Cochran et al. hypothesized that the C-strand and CC′ loop of VISTA comprised functional epitopes for VSIG-3 binding.[16] VSIG-3 protein is a transmembrane protein that consists of an IgV segment and an IgC2 segment. However, to our knowledge, there is no experimental VSIG-3 structure available from a public database. Therefore, in this study, the predicted three-dimensional structure of VSIG-3 (Uniport ID: Q5DX21) was retrieved from the AlphaFold Protein Database. By mutating 14 possible residues to alanine, Liu et al. proposed that one or more residues from Ser31, Gln33, Leu64, Ser65, Asn66, Leu112, Ser113, Asp114, Thr115, Gly116, Gly137, Leu138, Thr139, and Val140 of VSIG-3 may contribute to the interaction with VISTA.[25] Therefore, according to the mutagenesis studies, we deduced that the VISTA front face composed of G-, F-, C′-, and C-strands, and the VSIG-3 back face composed of C-, C′-, C″-, F-, and G-strands formed the interfaces of the VISTA/VSIG-3 complex (Figure 2).

3.2. VISTA/VSIG-3 Complex Models. A total of 2000 VISTA/VSIG-3 complex models were obtained by the ZDOCK protein−protein docking method, and 439 of them were selected for further analysis as their interfaces consistent with our assumption (Figure S1). The docking poses were ranked by ZRank scores, ranging from 46.5 to −83.5 kcal/mol (Figure 3). Due to the homology and structural similarity of

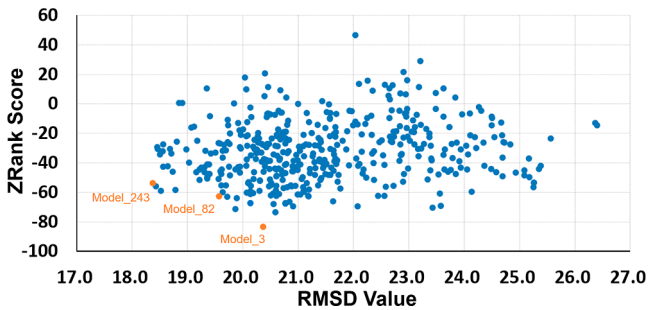

Figure 3. RMSD values versus ZRank scores of VISTA/VSIG-3 docking models.

VISTA/VSIG-3 with PD-1/PD-L1, the 439 docking models were aligned to the PD1/PD-L1 complex (PDB: 4ZQK), and the RMSD values between VISTA/VSIG-3 models and the PD1/PD-L1 complex were calculated. As shown in Figure 3, the RMSD values with respect to the PD1/PD-L1 complex vary between 18 and 27 Å in the VISTA/VSIG-3 models, among which model_3 has the lowest ZRank score of −83.5 kcal/mol, while the RMSD value was moderate (20.4 Å). Model_243 was the one that was the most similar to the PD-1/PD-L1 complex with an RMSD of 18.4 Å, while the ZRank

https://doi.org/10.1021/acsomega.4c07757
ACS Omega 2024, 9, 48657−48669

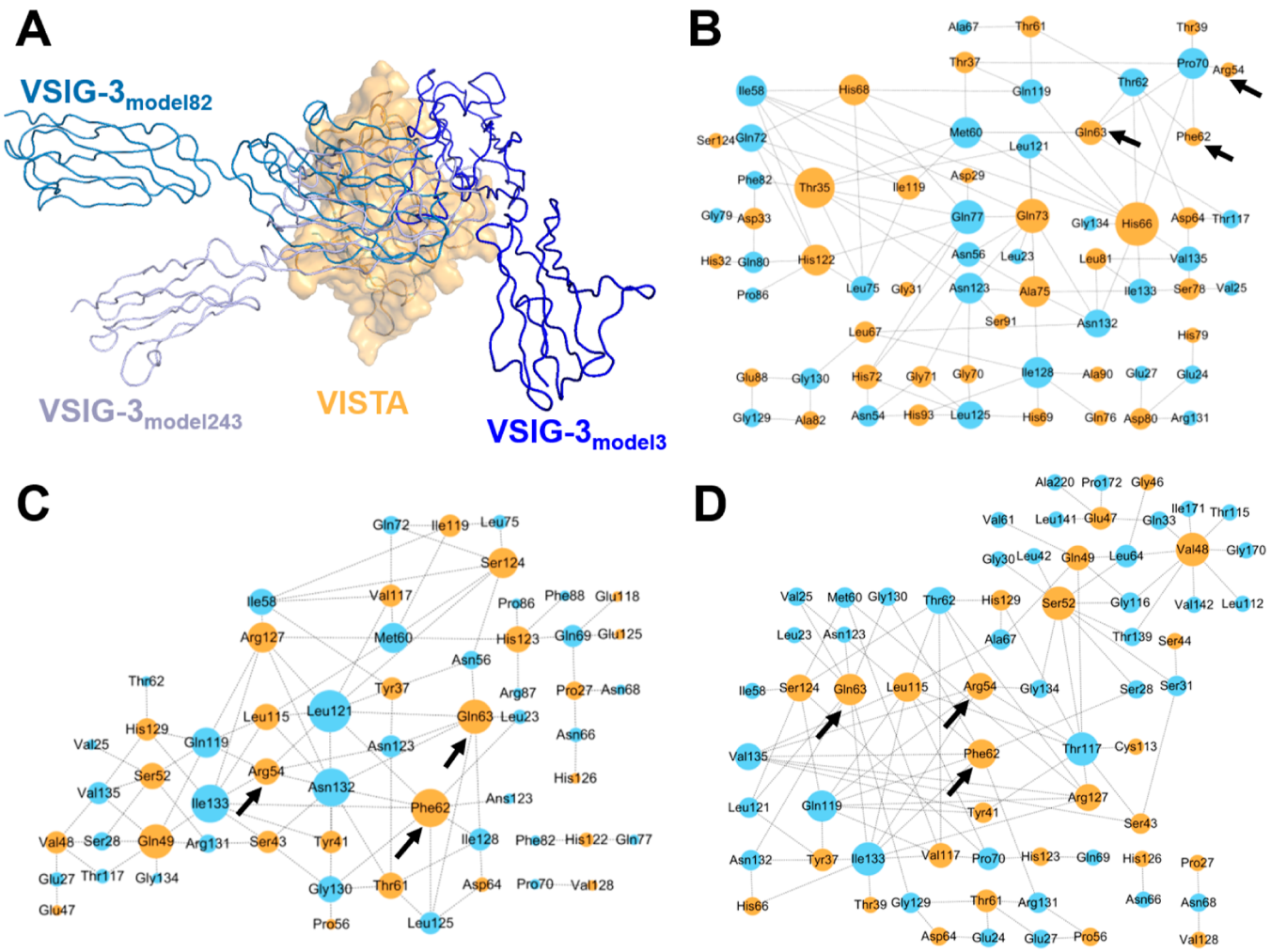

Figure 4. Interactive interfacial residues involved in VISTA/VSIG-3 models. (A) Alignment of the three complex models based on VISTA to show the different zones of VISTA surface for VSIG-3 binding. VISTA and VSIG-3 are shown in transparent surface and tube. The RIN maps for the models of the VISTA/VSIG-3 complex: (B) model_3, (C) model_82, and (D) model_243. Residues of VISTA and VSIG-3 are colored orange and light blue, respectively.

score (−54.0 kcal/mol) was much higher than that of model_3. There were also several models with balanced docking scores and RMSD values. Among them, model_82 was a representative one with a ZRank score of −62.9 kcal/mol and an RMSD value of 19.6 Å. Therefore, we further inspected the interfacial RINs of model_3, model_82, and model_243.

The interfacial RINs of the VISTA/VSIG-3 models, depicted using nodes and edges, were analyzed to study the VISTA structural epitopes (Figure 4). For all of the three models, the three possible epitopes ($Arg54_{VISTA}$, $Phe62_{VISTA}$, and $Gln63_{VISTA}$) of VISTA that were explored by triple mutant were involved in the interfacial interactions, though their contributions vary in the three models. In model_3, the three residues were located at the edge of the interface and participated in the least interactions (Figure 4B). In contrast, the three residues play more crucial roles and made more interactions with VSIG-3 in both model_82 and model_243 (Figure 4B,C). The cumulative count of interfacial interaction residues was 65 for model_3 (VISTA: 34 and VSIG-3:31), 58 for model_82 (VISTA: 26 and VSIG-3:32), and 68 for model_243 (VISTA: 27 and VSIG-3:41) (Table S1). Among the interfacial residues, 8 out of the 14 VSIG-3 residues which were identified as potentially important in mutant studies were observed in model_243, including $Ser31_{VSIG-3}$, $Gln33_{VSIG-3}$, $Leu64_{VSIG-3}$, $Asn66_{VSIG-3}$, $Leu112_{VSIG-3}$, $Thr115_{VSIG-3}$, $Gly116_{VSIG-3}$, and $Thr139_{VSIG-3}$, while only one of the mutant residues, $Asn66_{VSIG-3}$, was observed in the interaction networks of model_82 (Table S1), and none was observed in model_3. Nevertheless, compared to that of other models, in model_3, VSIG-3 interacted more heavily with the C strand of VISTA, which was confirmed to be a crucial strand in the work by Cochran et al.[17] Considering all three models, it was observed that VSIG-3 interacted with residues spanning the entire front face of the VISTA protein (Figures 4A and S2). Therefore, all three models were retained and subjected to classical MD simulations to unveil potential interactions between VISTA and VSIG-3.

3.3. Analysis of MD Trajectories. Conformational changes were sampled with three 800 ns simulations starting from the three VISTA/VSIG-3 complex models (model_3, model_82, and model_243) and with an additional 800 ns simulation starting from the unbound VISTA protein ($VISTA_{apo}$). Initially, the whole protein was aligned to the reference frame zero. The equilibration of MD trajectories was assessed by monitoring the convergence of RMSD plots for each frame relative to the initial structurally minimized

https://doi.org/10.1021/acsomega.4c07757
ACS Omega 2024, 9, 48657−48669

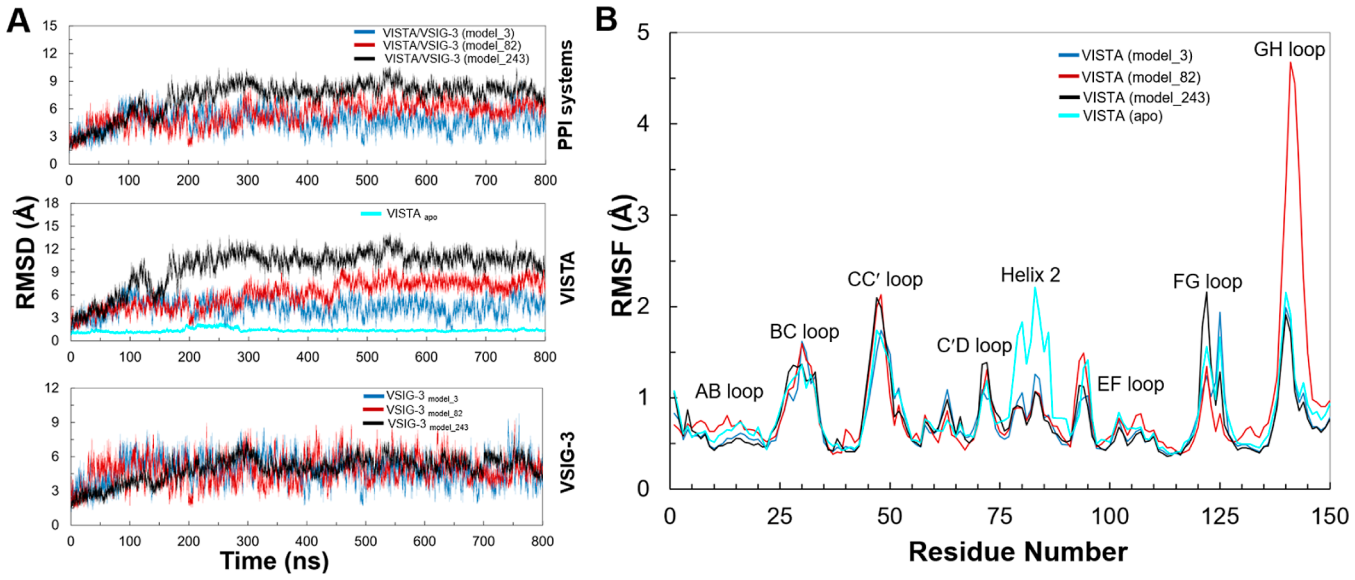

Figure 5. MD simulations (800 ns) of the VISTA systems. (A) Plots show the RMSD evolution values of backbone atoms with time (ns) for VISTA/VSIG-3 PPI systems (upper), VISTA protein in bound and unbound states (middle), and VSIG-3 protein in bound states (lower). (B) RMSF (Cα) per-residue values of VISTA during the MD simulation time.

Table 1. Binding Free Energies (Mean ± SD, kcal/mol) for Each VISTA/VSIG-3 Complex Model Calculated by MM/PBSA Methods

contribution		model_3	model_82	model_243
$\Delta E_{internal}$		0	0	0
ΔE_{vdw}		−124.05 ± 7.00	−91.11 ± 10.01	−92.45 ± 10.00
ΔE_{ele}		−88.39 ± 22.81	−124.51 ± 26.13	−192.19 ± 45.89
ΔE_{PB}		139.74 ± 17.06	165.94 ± 26.03	225.79 ± 36.28
$\Delta E_{nonpolar}$		−12.34 ± 0.51	−10.07 ± 1.08	−11.03 ± 0.70
ΔE_{MM}	$\Delta E_{internal} + \Delta E_{vdw} + \Delta E_{ele}$	−212.44 ± 24.07	−215.62 ± 30.70	−284.64 ± 43.71
ΔE_{solv}	$\Delta E_{PB} + \Delta E_{nonpolar}$	127.40 ± 16.85	155.24 ± 25.29	214.75 ± 36.08
ΔH	$\Delta E_{MM} + \Delta E_{solv}$	−85.04 ± 11.41	−60.38 ± 10.00	−69.89 ± 12.20
$-T\Delta S$		54.12	47.76	52.84
ΔG_{bind}	$\Delta H - T\Delta S$	−30.92	−12.62	−17.05

conformation (Figure 5A). Our observations showed that the unbound VISTA molecule exhibited rapid stabilization, whereas VISTA as a receptor protein in VISTA/VSIG-3 complex systems displayed pronounced fluctuations before reaching stability after 300 ns of MD simulations. In comparison to $VISTA_{apo}$, which displayed an average RMSD value of 1.4 Å, $VISTA_{model\_3}$, $VISTA_{model\_82}$, and $VISTA_{model\_243}$ exhibited significantly higher average backbone deviations of 4.4, 6.1, and 9.7 Å, respectively. In the case of binding partner, the protein backbone of VSIG-3 exhibited a consistently significant amplitude throughout the entire dynamic simulation process in model_3 and model_82, whereas it stabilized with minimal backbone fluctuations after 300 ns in model_243. Collectively, the results indicated that the constructed models underwent significant structural deviations during simulations to generate more reasonable conformations. The variations were further elucidated through the calculation of RMSF values, which provided insights into the local fluctuations occurring at the Cα atomic level of VISTA in both bonded and unbonded systems.

As observed in Figure 5B, in both of the bounded and unbounded systems, VISTA followed similar trends, and the Cα fluctuations mainly occurred in loop regions, while the core of VISTA has minimal fluctuations. In the presence of VSIG-3, the $RMSF_{avg}$ values of $VISTA_{model\_3}$ (0.26 Å), $VISTA_{model\_82}$ (0.87 Å), and $VISTA_{model\_243}$ (0.76 Å) were similar or slightly decreased as compared to that of $VISTA_{apo}$ (0.84 Å). The C_α atoms in the AB and EF loops were observed to have the least fluctuations in simulated $VISTA_{apo}$, while BC, CC′, FG, and GH loops have higher fluctuations. Similar zones of fluctuations were observed in the constructed models. However, it was noticed that helix 2 of $VISTA_{apo}$ had a much higher fluctuation when compared to $VISTA_{VSIG-3}$. Unexpectedly, an increased fluctuation was observed for the GH loop in the $VISTA_{model\_82}$-simulated structure compared to $VISTA_{apo}$. Overall, compared to the apo form, the binding of VSIG-3 resulted in a reduction of fluctuation in helix 2, with other regions maintaining similar fluctuation patterns. Finally, a timeline was produced to visually represent the conformational variations observed over the 800 ns simulations, showing that the β-sheets of VISTA protein were well aligned, and similar zones of fluctuations were observed consistent with RMSF profiles (Figure S3).

3.4. Analysis of Binding Free Energies. In the next step of our study, the MM-PBSA method was used for the calculation of the binding free energy for the three VISTA/VSIG-3 complex models. The MM-PBSA free energy for individual model was reported in Table 1. We observed that

https://doi.org/10.1021/acsomega.4c07757
ACS Omega 2024, 9, 48657−48669

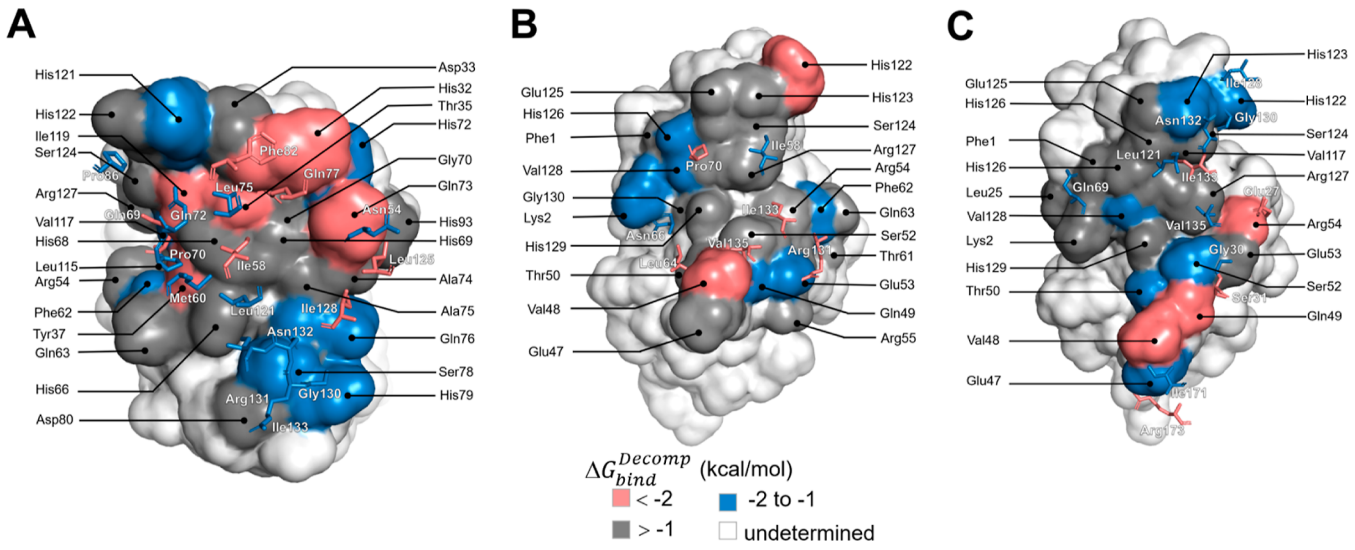

Figure 6. Surface representation of VISTA colored by per-residue decomposition energy with VSIG-3. (A) $VISTA_{model\_3}$, (B) $VISTA_{model\_82}$, and (C) $VISTA_{model\_243}$. The surfaces of VISTA are displayed with residues labeled in black and colored on the surface, while VSIG-3 in each model was shown as stick with its residues labeled white. Interfacial residues are colored according to ΔG_{bind}^{Decomp} values: red, <−2 kcal/mol; blue, −2 to −1 kcal/mol; dark gray, >−1 kcal/mol; light gray, undetermined. The coloring was the same for both the surface and the stick representations.

the formation of the VISTA complex was primarily driven by nonpolar contributions (Table S2). This may be due to nonpolar residues displacing water molecules from the interface and becoming buried. However, we also noted that the electrostatic energy contributed favorably to the binding affinity in the models. This is because PPIs cannot be solely driven by nonpolar interactions. Instead, charged residues located at the interface play a crucial role in providing specificity and ligand recognition through electrostatic interactions.[26]

The favorable binding free energies were primarily based on the individual energy terms of van der Waals interactions (ΔE_{vdw}) and the nonpolar solvation contribution ($\Delta E_{nonpolar}$), resulting from the burial of hydrophobic groups at the interfaces. The van der Waals energy exhibited values of −124.05 ± 7.00 kcal/mol for model_3, −91.11 ± 10.01 kcal/mol for model_82, and −92.45 ± 10.00 kcal/mol for model_243, respectively, while $\Delta E_{nonpolar}$ contributed only approximately −10 kcal/mol to the binding affinity. The contributions of electrostatic forces to the binding free energy were represented by the coulomb potential energy (ΔE_{ele}) with values of −88.39 ± 22.81, −124.51 ± 26.13, and −192.19 ± 45.89 kcal/mol and the PB solvation energy (ΔE_{polar}) with values of 139.74 ± 17.06, 165.94 ± 26.03, and 225.79 ± 36.28 kcal/mol for $VISTA_{model\_3}$, $VISTA_{model\_82}$, and $VISTA_{model\_243}$, respectively. However, for all three models, the combination of these two contributions was unfavorable for binding, as they exhibited opposing effects.

The enthalpy (ΔH or $\Delta G_{bind}^{substoal}$) of the systems was determined by considering the sum of polar and nonpolar interactions, without accounting for the entropy term ($-T\Delta S$). It is well known that entropy has a negative effect on the free energy of binding, which means that the final binding free energy (ΔG_{bind}) is always less favorable than the enthalpy (ΔH). In the specific complex under investigation, an estimation revealed that the entropy contributed approximately 54.12, 47.76, and 52.84 kcal/mol to the total binding energy in model_3, model_82, and model_243, respectively. However, in practical applications, due to the prohibitively high computational cost and relatively low prediction accuracy associated with the NMODE analysis, the entropy change is always neglected.

The total binding free energies of model_3, model_82, and model_243 were −30.92, −12.62, and −17.05 kcal/mol, respectively. Kalabokis et al. and Cochran et al. reported that the K_D values for VISTA/VSIG-3 ranged from 3.4 nM to 2 μM.[12,16] The experimental $\Delta G_{bind,exe}$ was estimated to range from −7.5 to −3.7 kcal/mol according to the formula $\Delta G_{bind} = -RT \ln K_A$. Obviously, the calculated ΔG_{bind} value of model_82 was close to the experimental $\Delta G_{bind,exe}$ value, while the other two models seem to be overestimated.

3.5. Energy Decomposition Analysis of the VISTA/VSIG-3 Complex. To gain insights into the contributions of crucial residues in determining the association of VISTA with VSIG-3, the binding free energy was decomposed at the residue level for the constructed models. The decomposition energy (ΔG_{bind}^{Decomp}) includes all components of the MM-PBSA free energy, except for entropy. The residues having energy contributions ≤ −1.00 kcal/mol were considered to have a more significant impact on the binding of two protein partners (Table S2). The spatial distributions of the VISTA key residues are displayed in Figure 6.

As displayed in Figure 6, the high-energy-contributing residues on VISTA were lesser than the ones observed from the RINs of the constructed models of the VISTA/VSIG-3 complex. It was observed that the key residues on $VISTA_{model\_3}$ were mainly located at C strand (Val34, Thr35, and Tyr37), F strand (Val117 and Ile119), and C′D loop (His72, Gln73, Gln76, Ser78, and His79). The residues His32, Thr35, Tyr37, Gln73, and Ile119 on $VISTA_{model\_3}$ showed the strongest interaction energy (Figure 6A). Key residues of $VISTA_{model\_82}$ were mainly located at the CC′ loop (Val48, Gln49, Glu53, and Phe62), FG loop (His122), and G strand (His126 and Val128). The residues Val48 and His122 on $VISTA_{model\_82}$ showed the strongest interaction energy (Figure 6B, Table S2). However, for $VISTA_{model\_243}$, the most critical residues were clustered on the CC′ loop (Val48, Gln49, and Arg54), contributing −14.65 kcal/mol to the total ΔG_{bind} (Figure 6C).

https://doi.org/10.1021/acsomega.4c07757
ACS Omega 2024, 9, 48657−48669

Table 2. Computational Alanine Scanning Results ($\Delta\Delta G_{bind}$, kcal/mol) of Key Residues Identified at VISTA Interfaces in Different VISTA/VSIG-3 Models

model_3		model_82		model_243	
residues	$\Delta\Delta G_{bind}$	residues	$\Delta\Delta G_{bind}$	residues	$\Delta\Delta G_{bind}$
His32	2.17 ± 1.35	Lys2	0.77 ± 1.62	Glu47	5.32 ± 5.10
Thr35	6.10 ± 2.82	Val48	2.03 ± 0.84	Val48	1.50 ± 1.01
Tyr37	2.60 ± 1.48	Gln49	0.90 ± 0.37	Gln49	3.59 ± 5.50
Phe62	0.34 ± 0.96	Glu53	9.44 ± 4.55	Thr50	0.35 ± 1.12
His72	1.47 ± 2.52	Arg54	2.18 ± 4.09	Ser52	1.90 ± 2.12
Gln73	5.51 ± 4.42	Phe62	0.77 ± 1.15	Glu53	3.79 ± 5.41
Gln76	1.41 ± 0.95	Gln63	0.97 ± 0.87	Arg54	8.87 ± 5.26
Ser78	0.52 ± 1.29	His122	3.35 ± 2.96	His122	1.98 ± 1.04
His79	0.91 ± 1.45	His126	2.34 ± 1.10	His123	1.65 ± 1.41
Val117	2.02 ± 2.12	Val128	1.85 ± 1.01	Val128	1.26 ± 1.22
Ile119	1.43 ± 0.86				
His121	1.31 ± 2.58				

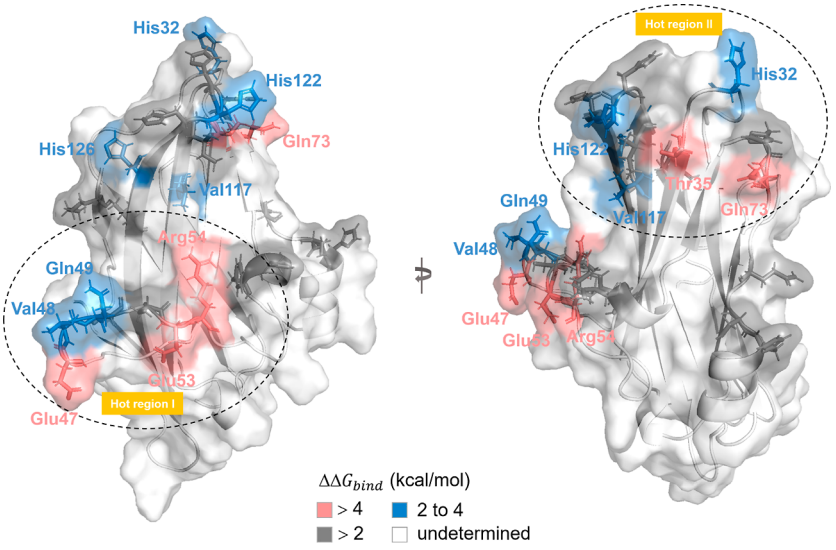

Figure 7. Ensemble hotspots of VISTA based on the changes in free energy after mutating the residue to alanine in the three models. Interfacial residues and their labels were colored according to $\Delta\Delta G_{bind}$ values: red, >4 kcal/mol; blue, 2 to 4 kcal/mol; dark gray, >2 kcal/mol; light gray, undetermined. The two hot regions were circled by dashed lines.

Based on their polar and nonpolar contributions, the interfacial residues from the energy decomposition analysis were further scrutinized. The total binding free energies of the majority of residues were primarily influenced by higher nonpolar energy contributions contributed by van der Waals interactions compared to the polar components, including coulomb potential energy and PB solvation energy. For some residues, the favorable electrostatic interactions were disfavored by polar solvation free energies such as His32, Arg54, and Arg127 in $VISTA_{model\_3}$; Lys2, Val48, Gln49, Phe62, His122, and Arg127 in $VISTA_{model\_82}$; and Val48, Gln49, Arg54, and His122 in $VISTA_{model\_243}$. However, some residues showed favorable polar energy contributions to the total binding energies of residues such as Asp33 and Asp80 ($VISTA_{model\_3}$); Glu53 ($VISTA_{model\_82}$) and Glu47 ($VISTA_{model\_243}$) (Table S2).

According to the distribution of residues, it was observed that the key amino acids on $VISTA_{model\_3}$ cluster spatially, forming a critical region which comprised His32, Thr35, Gln73, and Ile119, contributing the highest cumulative energy of −9.44 kcal/mol to ΔG_{bind} (Figure 6A). However, for model_82 and model_243, the CC′ and FG loops were the common interaction zones on VISTA in both models. Four residues, including Val48, Gln49, His122, and Val128, were found in common to have energy values less than −1.00 kcal/mol among the two models (Figure 6B,C).

3.6. Hotspot Validation through Computational Alanine Scanning. To verify the putative critical residues identified by binding energy decomposition, we calculated the binding free-energy contribution of interfacial residues by an alanine scanning study. Based on residue conservation and side-chain proximity, the key residues identified from energy decomposition analysis (≤−1.00 kcal/mol) were selected for alanine scanning. The results defined by measuring the differences in the binding free energy ($\Delta\Delta G_{bind}$) between each mutant type and wild type are exhibited in Table 2. The positive and negative values correspond to favorable and unfavorable contributions of the residues. If mutating a residue to alanine resulted in a decrease of 2 kcal/mol in binding affinity, then the residue should be considered as a hotspot.

In $VISTA_{model\_3}$, there were five key residues on $VISTA_{model\_3}$, His32, Thr35, Tyr37, Gln73, and Val117, as their mutation to alanine decreased the affinity by more than −2.00 kcal/mol. The interesting point was that despite there

https://doi.org/10.1021/acsomega.4c07757
ACS Omega 2024, 9, 48657−48669

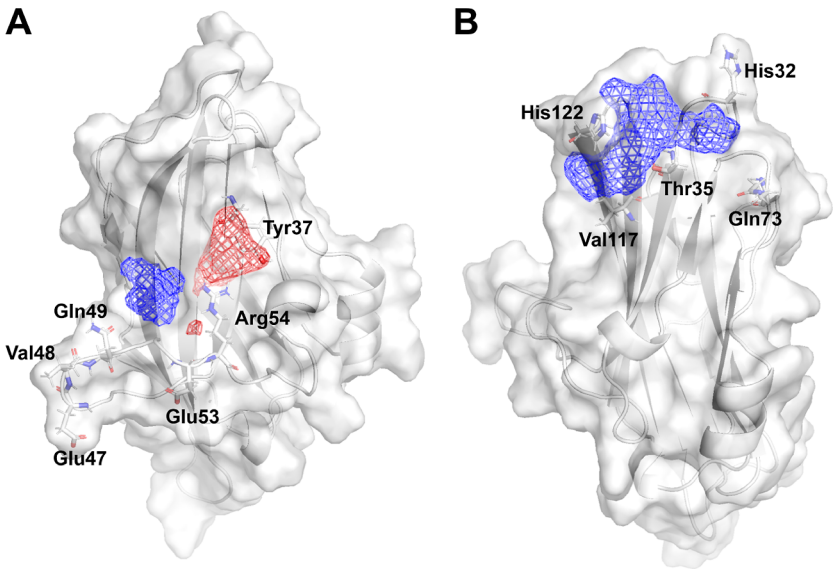

Figure 8. Analysis of VISTA hot regions using TRAPP: (A) hot region I and (B) hot region II. Transient subpockets that appear or disappear in at least 50% of structures compared to the reference structure were depicted as red and blue surface contours, respectively.

being 12 interfacial residues that had a favorable energy contribution in the wild type, only a few residues had a significant effect on the binding energy after alanine substitution. Notably, Thr35 and Gln73 among these residues showed significant effects on binding affinity, causing a reduction in binding energy of 6.10 and 5.51 kcal/mol, respectively.

In $VISTA_{model\_82}$, the E53A mutation led to a significant decrease in binding energy with a $\Delta\Delta G_{bind}$ value of 9.44 kcal/mol because of its substantial involvement in hydrogen bonding. Interestingly, despite showing an unfavorable energy contribution in the wild-type state, the R54A mutation in $VISTA_{model\_82}$ reduced the binding energy by 2.18 kcal/mol, indicating that its intermolecular Coulomb interaction with VSIG-3 was crucial. Additionally, the mutation of nonpolar residues V48A and basic residues H122A and H126A significantly reduced the binding energy by more than 2.00 kcal/mol. Therefore, in $VISTA_{model\_82}$, five residues, including Val48, Glu53, Arg54, His122, and His126, were identified as key residues.

In $VISTA_{model\_243}$, four residues, Glu47, Gln49, Glu53, and Arg54 of VISTA, appeared to be essential for interacting with VSIG-3 residues as their mutation to alanine dropped the affinity by more than 2.00 kcal/mol. Specially, the E47A and R54A mutations had significant effects on the binding energy ($\Delta\Delta G_{bind}$ > 4 kcal/mol). Both residues are located at the CC′ loop of VISTA. The remaining five residues in VISTA (Val48, Thr50, Ser52, His122, His123, and Val128) displayed relatively small energetic contributions (2 > $\Delta\Delta G_{bind}$ > 0 kcal/mol).

3.7. Ensemble Hotspots of VISTA. Despite the uncertainty of the structure of the VISTA/VSIG-3 complex in the real world, from the residue-wise energy decomposition and computational alanine scanning results of the three VISTA/VSIG-3 models, we proposed that the functional epitopes on VISTA were His32, Tyr37, Thr35, Glu47, Val48, Gln49, Glu53, Arg54, Gln73, His122, and His126. The $\Delta\Delta G_{bind}$ value for each hotspot residue was above 2 kcal/mol in at least one of the three VISTA/VSIG-3 models, with Thr35, Glu47, Glu53, Arg54, and Gln73 being the predominant contributors ($\Delta\Delta G_{bind}$ > 4 kcal/mol) (Figure 7). The side chains of the residues are mainly polar and charged or uncharged, indicating potential salt bridge or hydrogen-bonding interactions with VSIG-3.

According to our calculation, Arg54 should be one of the most important hotspots, showing a fairly large contribution to the binding energy (model_243: $\Delta\Delta G_{bind}$ = 8.87 ± 5.26 kcal/mol). In the work by Cochran et al., Arg54 significantly perturbed the interaction with VSIG-3 when mutated to alanine, as defined by ∼80% drop in binding.[16] Additionally, consistent with the findings of Cochran et al., our calculations also identified Tyr37 and His122 as hotspot residues.[17] It should be noted that several residues that were missed in Cochran's work still had a high chance of being hotspots. For example, Glu53 showed the largest energy contribution among all of the interfacial residues according to our calculations, indicating that the residue was in high probability to be a hotspot. Our study showed that the loops of VISTA had the highest contribution to the interaction with VSIG-3, and side chains of the hotspots were mainly clustered, forming two hot regions. One hot region was centered on Glu53 from the CC′ loop (hot region I), and the other one was centered on Thr35 (hot region II) (Figure 7). The identification of the two hot regions on VISTA divided the VISTA's large interface area into two subzones that could be targeted individually for screening or designing of small molecules or peptides.

3.8. Transient Pockets around Hot Regions of VISTA. Clusters of hotspot residues can serve as promising starting points for small-molecule design. However, protein interfaces are usually large and planar without typical pockets for ligand binding, making it challengeable to identify "drug-like" molecules.[27] Therefore, in the next step of our study, we performed calculations of the shape and physical properties of the hot regions of VISTA to identify transient pockets or subpockets that can be exploited in ligand screening, using the TRAPP (*TRAnsient Pockets in Proteins*) tool.[23] The apo form of the VISTA crystal structure was selected as the "reference structure," and its MD trajectory was utilized to investigate the dynamic behavior of the defined hot regions using TRAPP.

https://doi.org/10.1021/acsomega.4c07757
ACS Omega 2024, 9, 48657−48669

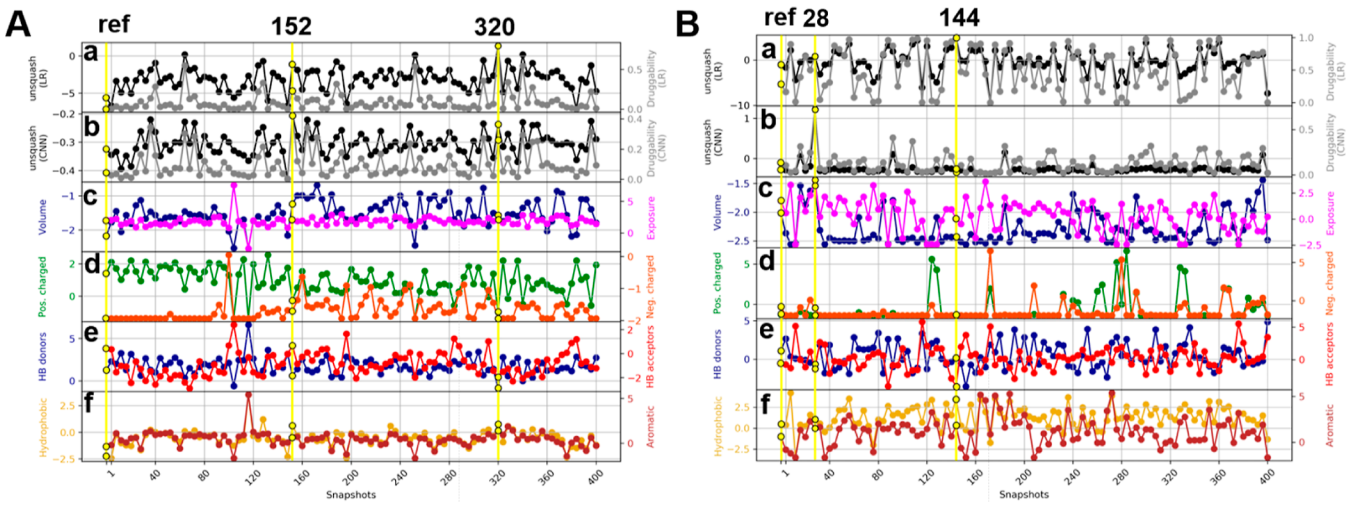

Figure 9. Physicochemical properties of the pockets in (A) hot region I and (B) hot region II along the MD trajectory. Panel (a,b) depict the variations in the LR and CNN druggability scores, respectively; (c−f) display the physicochemical properties used in the druggability models.

The VISTA protein features a relatively long CC′ loop spanning across the β-sheets and anchoring to the sheets via disulfide bonds between Cys54 and Cys113. Theoretically, the CC′ loop region should be able to form a suitable binding pocket for ligand binding due to the unevenness of the protein surface. After a sufficient period of MD simulation, transient pockets were found opening due to the movement of the amino acid residue side chains and the loop region. In the vicinity of hot region I proximal to the CC′ loop, transient regions, which were appearing/disappearing in at least 50% of structures relative to the reference structure, were represented by red and blue mesh, respectively (Figure 8A). The hot region II was a semiclosed domain that contained a relatively flat bottom formed by β-sheets which were surrounded by BC, C′D, and FG loops. In this region, transient subpockets that "disappear" in at least 50% of the snapshots were identified (Figure 8B). The opening of the transient pockets or subpockets provided grooves for ligand binding.

Identifying more druggable conformations and applying them effectively to drug discovery are of great significance for improving the success rate of drug development. Therefore, we continued to investigate the impact of conformational changes observed during MD simulations on the druggability of hot regions and their adjacent subpockets. In the TRAPP tool, druggability predictions are derived from two distinct models: one uses LR with a linear framework, relying on the generated global descriptors for the pocket; the other one employs a CNN that uses grid representation of the pocket to compute druggability scores.[21]

The variations in druggability score values (panels a and b) obtained from LR and CNN models for different conformations of the binding pocket in the vicinity of VISTA hot regions I and II along the MD trajectories are depicted in Figure 9A,B, respectively. Panels a and b clearly show the LR and CNN druggability score values computed for the pockets of reference structure, and panels c−f illustrate the variations in the values of the "global descriptors" that contribute to the LR model.

The determined reference pocket in region I showed very low druggability, with LR and CNN score values of 0.004 and 0.043, respectively (Figure 10A), while the values for the reference pocket in region II were 0.289 and 0.128, respectively (Figure 10D), indicating that hot region II might be more druggable for the drug design.

It was clear that certain snapshots exhibited significantly higher LR and CNN druggability score values compared with those computed for the reference pockets. In region I, the binding pockets with the highest LR and CNN druggability score values were observed in snapshots 320 and 152, respectively, with scores of 0.801 and 0.423 (Figure 10B,C). Additionally, when considering the summed druggability score values for their respective identified binding pockets, snapshot 320 demonstrated the highest cumulative score, with a value of 1.062. In the vicinity of hot region II, the found pockets of snapshots 144 and 28 had the highest LR and CNN druggability score values, measuring 0.992 and 0.726, respectively (Figure 10E,F). Furthermore, when the cumulative druggability score values for their respective identified binding pockets were considered, snapshot 28 displayed the highest summed scores, reaching a value of 1.433.

These results demonstrated that more druggable protein states, such as snapshot 320 for region I and snapshot 28 for region II, were generated during MD simulation. Snapshots displaying druggability scores exceeding those of the reference VISTA structure could potentially be utilized in the structure-guided development of new inhibitors targeting the protein.

4. DISCUSSION

In this research, models of the VISTA/VSIG-3 complex were constructed utilizing protein−protein docking based on the experimentally determined structure of VISTA and the AlphaFold-predicted structure of VSIG-3. The poses that resulted from protein−protein docking were further aligned to the PD-1/PD-L1 complex (PDB: 4ZQK) to help select the most reliable docking poses. Finally, three of the putative models, namely model_3, model_82, and model_243, were chosen for further MD simulations and binding energy analysis to map the binding hotspots in the VISTA protein surface.

In order to obtain reliable binding modes of the VISTA/VSIG-3 complex, the existing experimental data were utilized to set up protein−protein docking between VISTA and VSIG-3. Residues Arg54, Phe62, and Gln63 of the VISTA protein, which Cochran et al.[16] demonstrated to be key residues, were defined as binding sites in the docking study. However, the

https://doi.org/10.1021/acsomega.4c07757
ACS Omega 2024, 9, 48657−48669

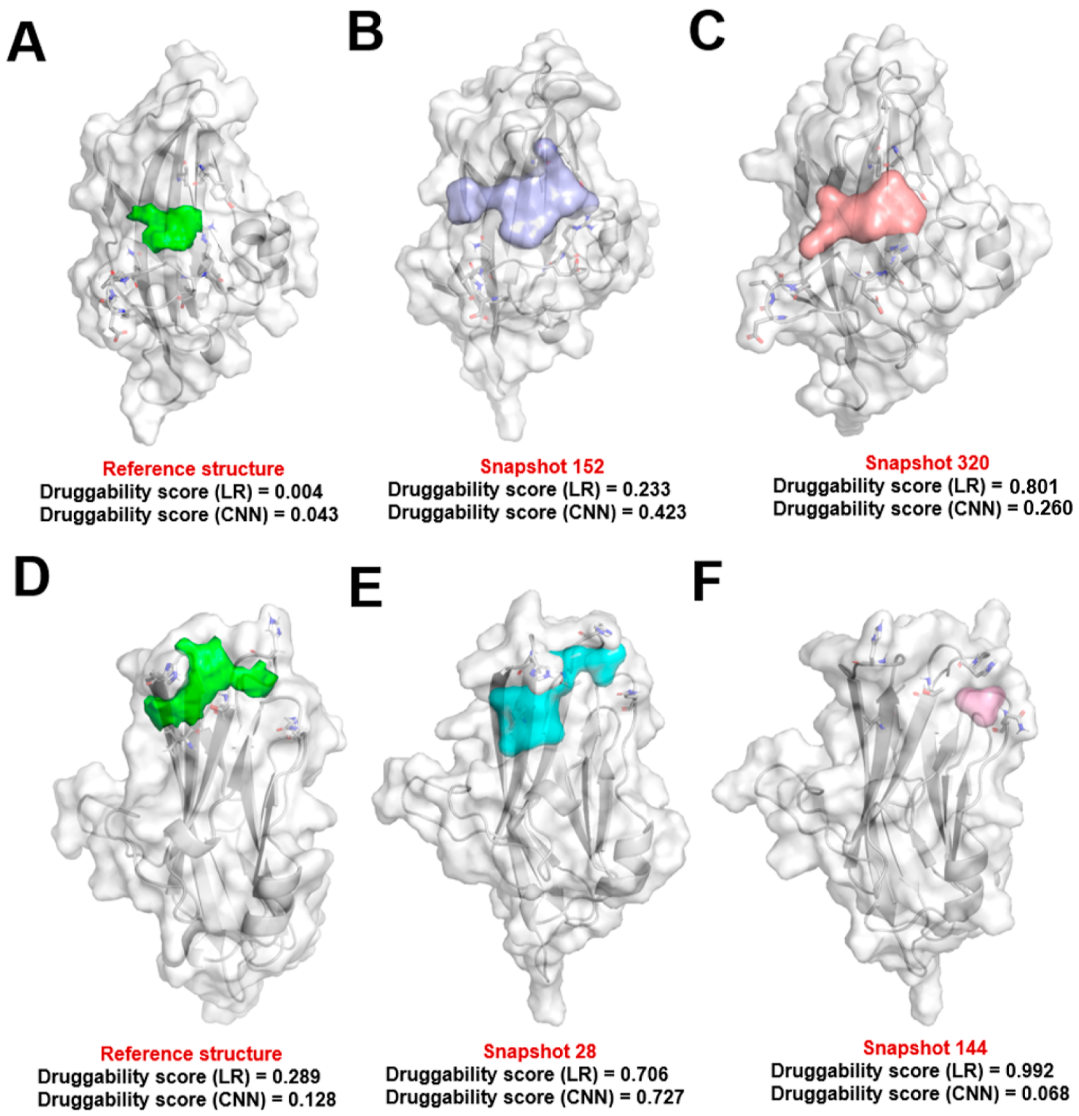

Figure 10. Visualization of pockets in the reference structure and representative snapshots. Pockets in the reference structure are shown as green surfaces in (A) hot region I and (D) hot region II. Conformational states of the transient pockets with high druggability scores as observed in (B) snapshots 152 (light blue surface) and (C) 320 (salmon surface) in region I and (E) snapshots 28 (cyan surface) and (F) 144 (magenta surface) in region II.

defining of the binding site on the VSIG-3 surface was difficult because of the limited experimental data. Though Liu et al. proposed that 14 residues of VSIG-3 might contribute to the interaction with VISTA,[25] the reduced binding affinity of VSIG-3 to VISTA following the mutations may be attributed to conformational changes in the surrounding regions (C-, C′-, C″-, F-, and G-strands of VSIG-3) rather than directly disrupting the contacts between VISTA and VSIG-3 interfaces, because all the 14 residues were mutated at the same time which would obviously affect the feature of the protein surface. Moreover, these residues are located at the bends between the front and back faces of the IgV domain and are difficult to interact with the VISTA protein due to the obstruction of the IgC domain (Figure 2B). Considering the reasons above, we defined VSIG-3 back face composed of C-, C′-, C″-, F-, and G-strands as the interface rather than defining the specific residues as the binding site.

The three VISTA/VSIG-3 complex models resulting from protein−protein docking experiments were subjected to MD simulations to evaluate their stability over time in a simulated aqueous environment, followed by free-energy calculation studies. We hope to derive the overall interaction landscape of VISTA/VSIG-3 from the selected models and integrate all data to identify all possible epitopes in the VISTA protein surface, which we called "ensemble hotspots" in this work. From residue-wise energy decomposition and computational alanine scanning results, we propose two crucial regions on VISTA that possess functional epitopes for VSIG-3 binding: the hot region I consists of residues Glu47, Val48, Gln49, Glu53, and Arg54, and hot region II consists of residues His32, Tyr37, Thr35, Gln73, His122, and His126 (Figure 7). In a recent study, Cochran et al. predicted Phe36, Tyr37, Lys38, Thr39, Arg54, Gln63, and His122 to be the epitopes on VISTA for VSIG-3 binding.[17] Surface exposure is a crucial requirement for a valid epitope, enabling interactions with the binding partner. However, the notably low surface exposure of Phe36, Lys38, and Thr39 raises concerns about their validity as potential epitopes. Therefore, based on the experimental data, only residues Tyr37, Arg54, Gln63, and His122 are theoretically shown to be hotspots in the VISTA surface. This is largely

https://doi.org/10.1021/acsomega.4c07757
ACS Omega 2024, 9, 48657−48669

consistent with our computational results, as all of the experimental hotspots were included in our calculated results, except for Gln63.

In the work by Cochran et al.,[17] Q63A mutation significantly affected VSIG-3 binding (>80% drop), whereas our calculation indicated that this mutation had no effect on the binding energy. A possible reason is that Gln63 is located at the edge of the interface and thereof does not form stable contacts with the interfacial residues of VSIG-3. Nonetheless, Gln63 is likely to play a role in stabilizing the located helix and adjacent CC′ loop of VISTA. Therefore, the decreased VISTA/VSIG-3 binding caused by Q63A mutation might be attributed to the change of the interfacial surroundings rather than the loss of contacts between residues in the interfaces of VISTA and VSIG-3.

Our study also provides new insights into the dynamics of the interface of VISTA. Using TRAPP for analyzing the conformational variations of the hot regions during our MD simulations of the apo structure of VISTA, binding pockets conserved in at least 50% of the analyzed snapshots were captured. Moreover, more druggable conformational states of the binding pockets than in the crystallographic structure were recognized among the snapshots of our MD simulations using the druggability scores in the TRAPP tool. The identified snapshots with druggable pockets should aid virtual screening and other structure-based approaches for the selection and design of novel VISTA/VSIG-3 inhibitors.

Finally, it must be emphasized that solving the structure of the VISTA/VSIG-3 complex via experimental methods like cryo-EM and X-ray crystallography is of major importance. Before that, our computational data can serve as a valuable complement to the existing experimental data. To the best of our knowledge, our study is pioneering in using computational methods for an analysis of the interfaces and hotspots between VISTA and VSIG-3.

5. CONCLUSIONS

In summary, the findings of this study have delineated critical residues located at the interfaces of the VISTA/VSIG-3 complex, with a specific focus on the potential hotspots situated on the VISTA interface that exert a substantial impact on the binding affinity with VSIG-3. The putative hotspots within the VISTA interface comprised residues His32, Tyr37, Thr35, Glu47, Val48, Gln49, Glu53, Arg54, Gln73, His122, and His126. Among these, Thr35, Glu47, Glu53, Arg54, and Gln73 appeared to be the most important ones. Moreover, we observed that the hotspots clustered to form two distinct regions, hot regions I and II, dividing VISTA's expansive interface area into two subzones suitable for individual targeting in the screening or design of small molecules or peptides. Furthermore, by using the TRAPP tool, "transient" subpockets were identified within each hot region during MD simulations of the apo structure of VISTA. We found two "transient" subpockets (an "appearing" subpocket and a "disappearing" subpocket) in hot region I, and they could merge into a larger binding pocket in some snapshots during MD simulation. In hot region II, the identified "transient" binding pocket was a "disappearing" binding pocket, which disappeared in at least 50% of the analyzed snapshots. On further analysis of the physicochemical properties of the pockets calculated by the TRAPP tool, we recognized VISTA conformational states with more druggable pockets in the hot regions than those in the experimental apo structure. As there is no VISTA/VSIG-3 complex structure reported yet, the findings presented in this study are anticipated to serve as a blueprint for the systematic development of agents targeting the VISTA/VSIG-3 immune checkpoint pathway in the future.

■ ASSOCIATED CONTENT

Data Availability Statement

All the data have been provided as Supporting Information. Protein docking files, representative snapshots from the trajectories, and all data files will be available in the Zenodo repository (10.5281/zenodo.11190436).

Supporting Information

The Supporting Information is available free of charge at https://pubs.acs.org/doi/10.1021/acsomega.4c07757.

Total of 439 docking poses of VISTA/VSIG-3 complex generated by ZDOCK; three constructed models of VISTA/VSIG-3 complex: model_3, model_82, and model_243; interfacial residues of VISTA/VSIG-3 models; conformational changes in the VISTA protein over 800 ns MD simulation; and energy contribution of individual amino acid residues on each of the VISTA/VSIG-3 interface calculated using the MM-PBSA method (PDF)

Accession Codes

VISTA: Q9H7M9 (VISTA_HUMAN). VSIG-3: Q5DX21 (IGS11_HUMAN)

■ AUTHOR INFORMATION

Corresponding Author

Jiqing Ye − *School of Pharmacy, Inflammation and Immune Mediated Diseases Laboratory of Anhui Province, Anhui Medical University, Hefei 230032, China;* orcid.org/0000-0003-2461-4325; Email: jiqing_ye@ahmu.edu.cn

Authors

Bingjie Li − *School of Pharmacy, Inflammation and Immune Mediated Diseases Laboratory of Anhui Province, Anhui Medical University, Hefei 230032, China*

Lixiu Xu − *School of Pharmacy, Inflammation and Immune Mediated Diseases Laboratory of Anhui Province, Anhui Medical University, Hefei 230032, China*

Chu Chen − *School of Pharmacy, Inflammation and Immune Mediated Diseases Laboratory of Anhui Province, Anhui Medical University, Hefei 230032, China*

Complete contact information is available at: https://pubs.acs.org/10.1021/acsomega.4c07757

Author Contributions

B.L. performed the molecular simulation and data analysis. L.X. checked the results. C.C. helped with the calculation and analyses. J.Y. proposed and designed the study and wrote the manuscript. All authors have read and approved the manuscript.

Notes

The authors declare no competing financial interest.

■ ACKNOWLEDGMENTS

This research project was supported by the Start-up Found from Anhui Medical University (grant no. 0601120201 for J.Y.) and Special Funding for Young Talents from Inflamma-

https://doi.org/10.1021/acsomega.4c07757
ACS Omega 2024, 9, 48657−48669

tion and Immune Mediated Diseases Laboratory of Anhui Province (grant no. 0601120202 for J.Y.).

REFERENCES

(1) Aragon-Sanabria, V.; Kim, G. B.; Dong, C. From cancer immunoediting to new strategies in cancer immunotherapy: the roles of immune cells and mechanics in oncology. *Biomechanics in Oncology*; Springer Cham, 2018; Vol. *1092*, pp 113−138.
(2) Tan, S.; Li, D.; Zhu, X. Cancer immunotherapy: Pros, cons and beyond. *Biomed. Pharmacother.* **2020**, *124*, 109821.
(3) (a) Darragh, L. B.; Karam, S. D. Amateur antigen-presenting cells in the tumor microenvironment. *Mol. Carcinog.* **2022**, *61* (2), 153−164. (b) Jhunjhunwala, S.; Hammer, C.; Delamarre, L. Antigen presentation in cancer: insights into tumour immunogenicity and immune evasion. *Nat. Rev. Cancer* **2021**, *21* (5), 298−312.
(4) (a) Kubli, S. P.; Berger, T.; Araujo, D. V.; Siu, L. L.; Mak, T. W. Beyond immune checkpoint blockade: emerging immunological strategies. *Nat. Rev. Drug Discovery* **2021**, *20* (12), 899−919. (b) He, X.; Xu, C. Immune checkpoint signaling and cancer immunotherapy. *Cell Res.* **2020**, *30* (8), 660−669. (c) Safarzadeh, A.; Alizadeh, M.; Beyranvand, F.; Falavand Jozaaee, R.; Hajiasgharzadeh, K.; Baghbanzadeh, A.; Derakhshani, A.; Argentiero, A.; Baradaran, B.; Silvestris, N. Varied functions of immune checkpoints during cancer metastasis. *Cancer Immunol. Immunother.* **2021**, *70*, 569−588.
(5) (a) Qin, S.; Xu, L.; Yi, M.; Yu, S.; Wu, K.; Luo, S. Novel immune checkpoint targets: moving beyond PD-1 and CTLA-4. *Mol. Cancer* **2019**, *18*, 155−214. (b) Kong, X. Discovery of new immune checkpoints: family grows up. *Regulation of Cancer Immune Checkpoints: Molecular and Cellular Mechanisms and Therapy*; Springer Nature, 2020; Vol. *1248*, pp 61−82.
(6) de Miguel, M.; Calvo, E. Clinical challenges of immune checkpoint inhibitors. *Cancer Cell* **2020**, *38* (3), 326−333.
(7) (a) Mitragotri, S.; Burke, P. A.; Langer, R. Overcoming the challenges in administering biopharmaceuticals: formulation and delivery strategies. *Nat. Rev. Drug Discovery* **2014**, *13* (9), 655−672. (b) Das, S.; Johnson, D. B. Immune-related adverse events and anti-tumor efficacy of immune checkpoint inhibitors. *J. Immunotherap. Cancer* **2019**, *7* (1), 306.
(8) Lines, J. L.; Sempere, L. F.; Broughton, T.; Wang, L.; Noelle, R. VISTA is a novel broad-spectrum negative checkpoint regulator for cancer immunotherapy. *Cancer Immunol. Res.* **2014**, *2* (6), 510−517.
(9) Gao, J.; Ward, J. F.; Pettaway, C. A.; Shi, L. Z.; Subudhi, S. K.; Vence, L. M.; Zhao, H.; Chen, J.; Chen, H.; Efstathiou, E.; et al. VISTA is an inhibitory immune checkpoint that is increased after ipilimumab therapy in patients with prostate cancer. *Nat. Med.* **2017**, *23* (5), 551−555.
(10) Yuan, L.; Tatineni, J.; Mahoney, K. M.; Freeman, G. J. VISTA: a mediator of quiescence and a promising target in cancer immunotherapy. *Trends Immunol.* **2021**, *42* (3), 209−227.
(11) Shekari, N.; Shanehbandi, D.; Kazemi, T.; Zarredar, H.; Baradaran, B.; Jalali, S. A. VISTA and its ligands: the next generation of promising therapeutic targets in immunotherapy. *Cancer Cell Int.* **2023**, *23* (1), 265.
(12) Wang, J.; Wu, G.; Manick, B.; Hernandez, V.; Renelt, M.; Erickson, C.; Guan, J.; Singh, R.; Rollins, S.; Solorz, A.; et al. VSIG-3 as a ligand of VISTA inhibits human T-cell function. *Immunology* **2019**, *156* (1), 74−85.
(13) Zheng, S.; Zhang, K.; Zhang, X.; Xiao, Y.; Wang, T.; Jiang, S. Development of Inhibitors Targeting the V-Domain Ig Suppressor of T Cell Activation Signal Pathway. *J. Med. Chem.* **2022**, *65* (18), 11900−11912.
(14) Tagliamento, M.; Agostinetto, E.; Borea, R.; Brandão, M.; Poggio, F.; Addeo, A.; Lambertini, M. VISTA: a promising target for cancer immunotherapy? *ImmunoTargets Ther.* **2021**, *10*, 185−200.
(15) Ghouzlani, A.; Lakhdar, A.; Rafii, S.; Karkouri, M.; Badou, A. The immune checkpoint VISTA exhibits high expression levels in human gliomas and associates with a poor prognosis. *Sci. Rep.* **2021**, *11* (1), 21504.
(16) Mehta, N.; Maddineni, S.; Mathews, I. I.; Andres Parra Sperberg, R.; Huang, P.-S.; Cochran, J. R. Structure and functional binding epitope of V-domain Ig suppressor of T cell activation. *Cell Rep.* **2019**, *28* (10), 2509−2516.e5.
(17) Mehta, N.; Maddineni, S.; Kelly, R. L.; Lee, R. B.; Hunter, S. A.; Silberstein, J. L.; Parra Sperberg, R. A.; Miller, C. L.; Rabe, A.; Labanieh, L.; et al. An engineered antibody binds a distinct epitope and is a potent inhibitor of murine and human VISTA. *Sci. Rep.* **2020**, *10* (1), 15171.
(18) (a) De Vivo, M.; Masetti, M.; Bottegoni, G.; Cavalli, A. Role of molecular dynamics and related methods in drug discovery. *J. Med. Chem.* **2016**, *59* (9), 4035−4061. (b) Wang, E.; Sun, H.; Wang, J.; Wang, Z.; Liu, H.; Zhang, J. Z.; Hou, T. End-point binding free energy calculation with MM/PBSA and MM/GBSA: strategies and applications in drug design. *Chem. Rev.* **2019**, *119* (16), 9478−9508.
(19) (a) Mittal, L.; Srivastava, M.; Kumari, A.; Tonk, R. K.; Awasthi, A.; Asthana, S. Interplay among structural stability, plasticity, and energetics determined by conformational attuning of flexible loops in PD-1. *J. Chem. Inf. Model.* **2021**, *61* (1), 358−384. (b) Ding, H.; Liu, H. Mapping the binding hot spots on human programmed cell death 1 and its ligand with free-energy simulations. *J. Chem. Inf. Model.* **2019**, *59* (10), 4339−4349. (c) Mittal, L.; Tonk, R.; Awasthi, A.; Asthana, S. Traversing through the dynamic protein−protein interaction landscape and conformational plasticity of PD-1 for small-molecule discovery. *J. Med. Chem.* **2022**, *65* (8), 5941−5953.
(20) (a) Stank, A.; Kokh, D. B.; Horn, M.; Sizikova, E.; Neil, R.; Panecka, J.; Richter, S.; Wade, R. C. TRAPP webserver: predicting protein binding site flexibility and detecting transient binding pockets. *Nucleic Acids Res.* **2017**, *45* (W1), W325−W330. (b) Yuan, J.-H.; Han, S. B.; Richter, S.; Wade, R. C.; Kokh, D. B. Druggability assessment in TRAPP using machine learning approaches. *J. Chem. Inf. Model.* **2020**, *60* (3), 1685−1699.
(21) Kokh, D. B.; Richter, S.; Henrich, S.; Czodrowski, P.; Rippmann, F.; Wade, R. C. TRAPP: A Tool for Analysis of Transient Binding Pockets in Proteins. *J. Chem. Inf. Model.* **2013**, *53*, 1235−1252.
(22) Clementel, D.; Del Conte, A.; Monzon, A. M.; Camagni, G. F.; Minervini, G.; Piovesan, D.; Tosatto, S. C. RING 3.0: fast generation of probabilistic residue interaction networks from structural ensembles. *Nucleic Acids Res.* **2022**, *50* (W1), W651−W656.
(23) Valdés-Tresanco, M. S.; Valdés-Tresanco, M. E.; Valiente, P. A.; Moreno, E. gmx_MMPBSA: A New Tool to Perform End-State Free Energy Calculations with GROMACS. *J. Chem. Theory Comput.* **2021**, *17* (10), 6281−6291.
(24) Collins, M.; Ling, V.; Carreno, B. M. The B7 family of immune-regulatory ligands. *Genome Biol.* **2005**, *6*, 223.
(25) Xie, X.; Chen, C.; Chen, W.; Jiang, J.; Wang, L.; Li, T.; Sun, H.; Liu, J. Structural basis of VSIG3: the ligand for VISTA. *Front. Immunol.* **2021**, *12*, 625808.
(26) Peczuh, M. W.; Hamilton, A. D. Peptide and protein recognition by designed molecules. *Chem. Rev.* **2000**, *100* (7), 2479−2494.
(27) Rooklin, D.; Wang, C.; Katigbak, J.; Arora, P. S.; Zhang, Y. AlphaSpace: fragment-centric topographical mapping to target protein−protein interaction interfaces. *J. Chem. Inf. Model.* **2015**, *55* (8), 1585−1599.

https://doi.org/10.1021/acsomega.4c07757
ACS Omega 2024, 9, 48657−48669